Mechanical mode ground-state cooling in an optomechanical system by modulating the driving field

Pengcheng Li(李鹏程)[1], Yang-Yang Wang(王洋洋)[2], and Lingyu Liu(刘玲妤)[1,†]

[1] *Faculty of Sciences, Civil Aviation Flight University of China, Guanghan* 618300, *China*

[2] *Shaanxi Engineering Research Center of Controllable Neutron Source, School of Electronic Information, Xijing University, Xi'an* 710123, *China*

(Received 9 May 2026; revised manuscript received 24 June 2026; accepted manuscript online 30 June 2026)

Ground-state cooling of a mechanical oscillator is a crucial prerequisite for exploring quantum effects in optomechanical systems, and its implementation is usually restricted to the weak-coupling and resolved-sideband regimes. To overcome this limitation, we propose a more experimentally feasible solution that relies on shaping both the amplitude and the frequency of the driving field in the primary cavity, without tuning the intercavity coupling or cavity frequencies. The frequency modulation maintains a persistent red-detuned regime that ensures preferential energy flow from the mechanical mode to the optical modes, while the auxiliary cavity accelerates the cooling without requiring high population. Numerical simulations using the chopped random basis optimization algorithm demonstrate nearly perfect ground-state cooling in the strong-coupling and unresolved-sideband regimes. A rigorous finite-time contraction theorem is proved, providing a strict upper bound on the final phonon number and guaranteeing the stability of the cooling process. The corresponding contraction factor reaches values as low as 10^{-6}. The scheme exhibits strong robustness to Gaussian white noise and spectral distortions, confirming its high experimental feasibility.

Keywords: optomechanical cooling, unresolved-sideband, strong-coupling, chopped random basis

PACS: 42.50.Wk, 42.50.Ct, 42.50.Pq, 02.60.Pn

DOI: 10.1088/1674-1056/ae843c **CSTR:** 32038.14.CPB.ae843c

1. Introduction

Optomechanical systems have been applied in areas ranging from basic laboratory research to precision measurement and quantum technology. For example, optomechanical measurement devices can surpass the standard quantum limit by exploiting quantum entanglement, squeezed states, quantum feedback, and back-action suppression. As a result, optomechanical measurements can achieve femtonewton-level force detection,[1] femtogram-level mass sensing,[2] and sub-picotesla magnetic field measurement.[3,4] Beyond these sensing applications, cooling mechanical modes to their quantum ground state is a central challenge in cavity optomechanics, as it enables the observation of macroscopic quantum phenomena such as superposition and entanglement.[5–8] Traditional sideband cooling[9–11] relies on resolving the motional sidebands, i.e., requiring the mechanical frequency ω_b to exceed the cavity decay rate κ (the resolved-sideband regime),[12] and typically operates in the weak-coupling limit.[13] While effective in specific configurations, this approach fails in the strong-coupling regime or under unresolved-sideband conditions, where instabilities arise and the rotating-wave approximation breaks down.[14,15] Alternative strategies — such as dissipative coupling,[16–18] feedback cooling,[19,20] squeezed-light enhancement,[10,21] sensing based on dressed states,[22] dark-mode control,[23] and coherent sensing of control errors[24] — have been explored, yet a universally robust and efficient method remains elusive.

In recent years, auxiliary systems such as an atomic ensemble[25] or a quantum well[26] have been incorporated into optomechanical systems. These methods can realize ground-state cooling by enhancing cooling and inhibiting heating via quantum interference. However, these methods usually require precise control of the coupling between the auxiliary system and the light field, which increases the experimental complexity. Alternatively, the stimulated Raman adiabatic passage (STIRAP)[27,28] and shortcuts to adiabaticity (STA) techniques[29–31] are also commonly used for mechanical ground-state cooling in optomechanics. There are two main implementations: one uses separate laser fields to independently control the primary and auxiliary cavities,[32] avoiding direct frequency modulation but requiring precise synchronization and phase stability. Another, proposed by Sarma *et al.*,[33] modulates both cavity frequencies and the drive amplitude in a tripartite system, achieving efficient cooling even in strong-coupling and unresolved-sideband regimes at the expense of complex electro-optic modulation. These two approaches thus represent a trade-off: one demands sophisticated multi-laser control, the other requires precise cavity-frequency modulation. However, the above requirements are challenging in practical experiments. For instance, it is hard to adjust the coupling strength between the optical cavities or the cavity frequency in on-chip optical cavity systems,[34,35] since the dis-

†Corresponding author. E-mail: liu_lingyu@cafuc.edu.cn

© 2026 Chinese Physical Society and IOP Publishing Ltd. All rights, including for text and data mining, AI training, and similar technologies, are reserved.

CPB Online In-Press

tance between cavities and the shape of each cavity are fixed after the fabrication is completed.

To overcome the above challenges and make the cavity-assisted methods easier to realize in experiments, in this paper, we present a theoretical framework for robust ground-state cooling of a mechanical oscillator by controlling only the input driving laser of the primary cavity. Our scheme offers three main advantages. First, by modulating only the amplitude and frequency of a single drive, our scheme is simpler than conventional approaches requiring dual-laser control or direct cavity-frequency tuning. Second, it achieves near-unity transfer efficiency over a wide parameter range, including the strong-coupling and unresolved-sideband regimes, via optimal control. Third, our scheme also has strong robustness to control noise and spectral distortions. Our work provides a practical route toward mechanical ground-state cooling in optomechanical systems, especially for on-chip optical systems.

2. Model

In a conventional optomechanical system, consisting of two cavity modes and a mechanical mode (b), the primary cavity mode is optomechanically coupled to the mechanical mode, with single-photon coupling rate g_{cb}, as shown in Fig. 1. The primary cavity (with mode c) is coupled to the auxiliary cavity (with mode a), with fixed coupling rate g_{ca}. The Hamiltonian of the complete system is given by (in units of $\hbar = 1$)

$$\begin{aligned} H \;=\; & \omega_a a^\dagger a + \omega_b b^\dagger b + \omega_c c^\dagger c \\ & + g_{cb} c^\dagger c (b + b^\dagger) + g_{ca}(a^\dagger c + c^\dagger a) \\ & + \mathrm{i}\left(\varepsilon_p(t) c^\dagger \mathrm{e}^{-\mathrm{i}\int_0^t \omega_p(t')\mathrm{d}t'} - \mathrm{H.c.}\right), \end{aligned} \tag{1}$$

where the first line describes the free Hamiltonians of the three modes and their mutual couplings, including the optomechanical interaction $g_{cb}c^\dagger c(b+b^\dagger)$ and the photon-hopping $g_{ca}(a^\dagger c + c^\dagger a)$. The a ($a^\dagger$), b ($b^\dagger$), and c ($c^\dagger$) denote the annihilation (creation) operators for the auxiliary cavity mode, mechanical mode, and primary cavity mode, with corresponding resonance frequencies ω_a, ω_b, and ω_c, respectively. The resonance frequencies of the two cavity modes, ω_a and ω_c, are time-independent. The second line represents the driving of the primary cavity, where both the amplitude $\varepsilon_p(t)$ and frequency $\omega_p(t)$ are time-dependent; these will serve as our control knobs. Under the transformation $R(t) = \exp\left[\mathrm{i}\phi(t)(a^\dagger a + c^\dagger c)\right]$, where $\phi = \int_0^t \omega_p(t')\mathrm{d}t'$, the Hamiltonian is given by

$$\begin{aligned} H \;=\; & (\omega_a - \omega_p(t))a^\dagger a + (\omega_c - \omega_p(t))c^\dagger c + \omega_b b^\dagger b \\ & + g_{cb} c^\dagger c (b + b^\dagger) + g_{ca}(a^\dagger c + c^\dagger a) \\ & + \mathrm{i}\left(\varepsilon_p(t) c^\dagger - \mathrm{H.c.}\right). \end{aligned} \tag{2}$$

The transformation $R(t)$ moves us into a frame rotating at the drive frequency $\omega_p(t)$, removing the explicit time dependence from the drive term. The resulting Hamiltonian now features time-dependent detunings $\omega_a - \omega_p(t)$ and $\omega_c - \omega_p(t)$, which can be tuned by chirping $\omega_p(t)$.

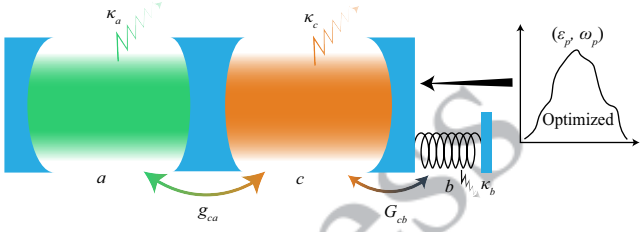


Fig. 1. Schematic of the cooling scheme for the optomechanical system, consisting of a primary optical cavity (mode c), an auxiliary optomechanical cavity (mode a), and a mechanical mode b. Mode a couples to mode c at a rate g_{ca}, while mode c couples to mode b at a tunable rate G_{cb} modulated by the optimized drive amplitude ε_p. The frequencies ω_a and ω_c of the two optical modes are modulated by the optimized drive frequency ω_p.

The dynamical behavior of the system operators is governed by the quantum Langevin equations

$$\begin{aligned} \dot{a} \;=\; & (-\mathrm{i}(\omega_a - \omega_p(t)) - \kappa_a)a - \mathrm{i}g_{ca}c + \sqrt{2\kappa_a}a_{\mathrm{in}}, \\ \dot{b} \;=\; & (-\mathrm{i}\omega_b - \kappa_b)b - \mathrm{i}g_{cb}c^\dagger c + \sqrt{2\kappa_b}b_{\mathrm{in}}, \\ \dot{c} \;=\; & (-\mathrm{i}(\omega_c - \omega_p(t)) - \kappa_c)c - \mathrm{i}g_{ca}a - \mathrm{i}g_{cb}c(b + b^\dagger) \\ & + \varepsilon_p + \sqrt{2\kappa_c}c_{\mathrm{in}}, \end{aligned} \tag{3}$$

where the parameters κ_a, κ_b, and κ_c are the loss rates for the auxiliary cavity mode, the mechanical mode, and the primary cavity mode, respectively. The associated noise operators a_{in}, b_{in}, and c_{in} have zero mean and satisfy the correlation functions, $\langle A_{\mathrm{in}}(t)A_{\mathrm{in}}^\dagger(t')\rangle = (\bar{n}_A + 1)\delta(t-t')$, $\langle A_{\mathrm{in}}^\dagger(t)A_{\mathrm{in}}(t')\rangle = \bar{n}_A\delta(t-t')$, where $\bar{n}_A = (\mathrm{e}^{\hbar\omega_A/k_{\mathrm{B}}T_{\mathrm{bath}}} - 1)^{-1}$ denotes the average thermal occupation number for mode A ($A = a, b, c$). Here T_{bath} is the temperature of the common thermal bath and k_{B} is Boltzmann's constant.

Under external driving, we adopt the standard linearization approach,[36,37] in which each Heisenberg operator is written as the sum of its steady-state mean value and a quantum fluctuation operator: $a = \alpha + a_1$, $b = \beta + b_1$, $c = \eta + c_1$, with α, β, η being the classical mean-field amplitudes and a_1, b_1, c_1 the corresponding fluctuation operators. Separating the classical and quantum parts yields both the classical and quantum Langevin equations

$$\begin{aligned} & -\mathrm{i}(\omega_a - \omega_p(t))\alpha - \mathrm{i}g_{ca}\eta - \kappa_a\alpha = 0, \\ & -\mathrm{i}\omega_b\beta - \mathrm{i}g_{cb}|\eta|^2 - \kappa_b\beta = 0, \\ & (-\mathrm{i}(\omega_c - \omega_p(t)) - \kappa_c)\eta - \mathrm{i}g_{ca}\alpha \\ & -\mathrm{i}g_{cb}\eta(\beta + \beta^*) + \varepsilon_p(t) = 0, \\ & \dot{a_1} = (-\mathrm{i}(\omega_a - \omega_p(t)) - \kappa_a)a_1 - \mathrm{i}g_{ca}c_1 + \sqrt{2\kappa_a}a_{\mathrm{in}}, \\ & \dot{b_1} = (-\mathrm{i}\omega_b - \kappa_b)b_1 - \mathrm{i}g_{cb}\eta(c_1^\dagger + c_1) \end{aligned} \tag{4}$$

CPB Online In Press

$$
\begin{aligned}
&-\mathrm{i}g_{cb}c_1^\dagger c_1+\sqrt{2\kappa_b}b_{\mathrm{in}},\\
\dot{c_1} =\ &(-\mathrm{i}(\omega_c-\omega_p(t))-g_{cb}(\beta+\beta^*)-\kappa_c)c_1\\
&-\mathrm{i}g_{ca}a_1-\mathrm{i}g_{cb}\eta(b_1+b_1^\dagger)\\
&-\mathrm{i}g_{cb}c_1(b_1+b_1^\dagger)+\sqrt{2\kappa_c}c_{\mathrm{in}}. \qquad (5)
\end{aligned}
$$

For the parameter regime considered in this work, the term $g_{cb}(\beta+\beta^*)$ is negligible compared to $\mathrm{i}(\omega_c-\omega_p(t))$ and can therefore be omitted. The mean-field amplitude of the primary cavity mode, η, is then given by

$$
\eta=\frac{\varepsilon_p(\mathrm{i}(\omega_a-\omega_p(t))+\kappa_a)}{g_{ca}^2+(\mathrm{i}(\omega_c-\omega_p(t))+\kappa_c)(\mathrm{i}(\omega_a-\omega_p(t))+\kappa_a)}. \qquad (6)
$$

In the quantum Langevin equations, the fluctuation product terms, such as $\mathrm{i}g_{cb}c_1^\dagger c_1$ and $\mathrm{i}g_{cb}c_1(b_1+b_1^\dagger)$, are negligibly small compared to the other terms and are therefore omitted. This leads to the linearized Hamiltonian of the system

$$
\begin{aligned}
H_{\mathrm{lin}} =\ &(\omega_a-\omega_p(t))a_1^\dagger a_1+(\omega_c-\omega_p(t))c_1^\dagger c_1+\omega_b b_1^\dagger b_1\\
&+G_{cb}(c_1+c_1^\dagger)(b_1+b_1^\dagger)\\
&+g_{ca}(a_1^\dagger c_1+c_1^\dagger a_1), \qquad (7)
\end{aligned}
$$

where $G_{cb}=\eta g_{cb}$ denotes the linearized optomechanical coupling strength, enhanced by coherent driving. Since η is proportional to the amplitude of the driving field ε_p, the coupling strength G_{cb} can be tuned by adjusting the external optical drive applied to cavity c. However, it should be noted that the cavity–cavity coupling g_{ca} cannot be modulated using this method. In the following analysis, we assume that G_{cb} can be time-modulated, while g_{ca} remains constant. We obtain the Hamiltonian in the interaction picture by applying the transformation $U=\exp[-\mathrm{i}\omega_b(a_1^\dagger a_1+c_1^\dagger c_1+b_1^\dagger b_1)t]$, where

$$
\begin{aligned}
H =\ &\delta_a(t)a_1^\dagger a_1+\delta_c(t)c_1^\dagger c_1+G_{cb}(t)\left(c_1^\dagger b_1+c_1 b_1^\dagger\right)\\
&+G_{cb}(t)\left(\mathrm{e}^{-2\mathrm{i}\omega_b t}c_1 b_1+\mathrm{e}^{2\mathrm{i}\omega_b t}c_1^\dagger b_1^\dagger\right)\\
&+g_{ca}\left(c_1^\dagger a_1+c_1 a_1^\dagger\right), \qquad (8)
\end{aligned}
$$

here $\delta_a(t)=\Delta_a-\omega_p(t)$ and $\delta_c=\Delta_c-\omega_p(t)$ are time-dependent detunings, and $\Delta_a=\omega_a-\omega_b$ and $\Delta_c=\omega_c-\omega_b$. These two detunings can be varied by modulating the drive frequency. Note that we have kept the counter-rotating terms $\mathrm{e}^{\pm 2\mathrm{i}\omega_b t}$ (originating from cb and $c^\dagger b^\dagger$) for completeness. In the usual rotating-wave approximation (RWA), these counter-rotating terms are neglected under the condition that the system operates in the resolved-sideband regime ($\kappa\ll\omega_b$) and weak-coupling limit ($G_{cb}\ll\omega_b,\kappa$). However, in the strong-coupling and unresolved-sideband regimes targeted by our scheme, these terms become significant. Our optimal control approach can potentially exploit or compensate for their effects, making the RWA unnecessary.

3. Population transfer protocol and robustness

3.1. Pulse optimization via CRAB

The time-dependent coupling is set to $G_{cb}(t)\equiv\Omega_p(t)/2$, and the static cavity–cavity coupling g_{ca} is constant and equal to $\Omega_p^{\max}/2$, where $\Omega_p^{\max}$ denotes the maximum value of $\Omega_p(t)$. By modulating the amplitude and frequency of the drive, the coupling rates $G_{cb}(t)$ and the two detunings can be modulated. Quantum optimal control theory offers a powerful framework for designing time-varying fields to steer quantum dynamics with high fidelity.[38–40] Among various algorithms, the chopped random basis (CRAB) method is particularly practical: it expands control pulses in a truncated basis of randomly selected frequencies, optimizing only a few coefficients under experimental constraints like bandwidth and amplitude limits.[41–43] CRAB has been successfully applied to state transfer, gate compilation, and entanglement synthesis across diverse platforms, and its extensions (e.g., dCRAB) accommodate open-system optimization.[44] Importantly, CRAB's flexibility in shaping both amplitude and frequency modulated pulses aligns naturally with our goal of implementing STIRAP-like transfer using a single drive field, thereby avoiding the complexities of dual-laser control or direct cavity modulation. We use CRAB to find the control signal profiles $\Omega_p(t)$ and circular frequency $\omega_p(t)$ as follows: first, an initial guess for the profiles $\Omega_{p_0}(t)$ and ω_{p_0} is made, then a correction to the initial pulse is sought in the following form:

$$
\Omega_p(t)=\Omega_{p_0}(t)(1+0.3G(t)),\ \omega_p(t)=\omega_{p_0}(1+0.2F(t)). \qquad (9)
$$

The functions $G(t)$ and $F(t)$ are expressed by a limited amount of spectral components K

$$
G(t)=\sum_{k=1}^{K}a_k g_k(\omega_k t),\ \ F(t)=\sum_{k=1}^{K}d_k g_k(\omega_k t), \qquad (10)
$$

where g_k denote some basis functions for a Fourier-type series expansion, a_k and d_k denote the coefficients associated with each basis function, and ω_k denote the angular frequencies. The basis frequency ω_k is randomized as follows:

$$
\omega_k=k\cdot\frac{2\pi}{T_{\mathrm{end}}-T_0}\cdot\left(1+\delta_k\right),\quad k=1,2,\ldots,K, \qquad (11)
$$

where $T_{\mathrm{end}}-T_0$ denotes the total duration of the control pulse. The random offsets δ_k are independently sampled from a uniform distribution $[-0.25,0.25]$. This multiplicative frequency jitter serves to break the strict harmonic structure, thereby mitigating overfitting to spurious periodicities and reducing the risk of the optimization becoming trapped in local minima associated with accidental resonances of the system.

Using the CRAB method, we optimized the control parameters of the Hamiltonian. This was done by employing a basis of 8 randomized sinusoidal and 8 randomized cosinusoidal functions for each parameter. In all our optimizations, we use a Gaussian pulse of the form $\Omega_{p_0}(t)=\Omega_0\mathrm{e}^{-(t-t_c)^2/\tau}$ as

CPB Online In Press

the initial ansatz. This shape is standard in STIRAP protocols, as its gradual turn-on adiabatically initiates population transfer without inducing unwanted excitations. The optimized pulse $\Omega_p(t)$ is scaled to ensure that its maximum amplitude satisfies $\Omega_{\max} \equiv \Omega_0$. The parameter ω_{p_0} is optimized using CRAB to determine its optimal value. This optimized value is subsequently held constant during the implementation of all control pulses.

3.2. Population transfer protocol

Under the RWA, the Hamiltonian (8) can be expressed as

$$H_{\rm RWA} = \begin{bmatrix} 0 & \Omega_p(t)/2 & 0 \\ \Omega_p^*(t)/2 & \delta_c(t) & g_{ca} \\ 0 & g_{ca} & \delta_a(t) \end{bmatrix}. \tag{12}$$

The evolution of the modal occupancies N_b, N_a, and N_c is shown in Fig. 2(a), for the initial condition $(N_b, N_a, N_c) = (1,0,0)$. This dynamics is computed by solving the Schrödinger equation with the CRAB-optimized control pulses. Figure 2(b) shows the profile of the amplitude $\Omega_p(t)$ and $\Omega_{p_0}(t)$. Figure 2(c) shows the frequency of $\omega_p(t)$ and ω_{p_0}. In describing the evolution, coupling to external baths was not considered. The population is transferred from the phonon b mode to the auxiliary cavity a mode with virtually 100% fidelity, while rarely leaking into the primary cavity c mode.

For a realistic implementation of our proposal, the dynamics must be treated within the framework of open quantum systems. In this context, the evolution of the phonon number is governed by the quantum master equation,[45] analyzable via covariance methods. Specifically for our model, the relevant master equation is

$$\begin{aligned} \dot{\rho} =& -\mathrm{i}[H,\rho] + \kappa_a(\bar{n}_a+1)\mathcal{D}[a_1]\rho + \kappa_a\bar{n}_a\mathcal{D}[a_1^\dagger]\rho \\ &+\kappa_c(\bar{n}_c+1)\mathcal{D}[c_1]\rho + \kappa_c\bar{n}_c\mathcal{D}[c_1^\dagger]\rho \\ &+\kappa_b(\bar{n}_b+1)\mathcal{D}[b_1]\rho + \kappa_b\bar{n}_b\mathcal{D}[b_1^\dagger]\rho, \end{aligned} \tag{13}$$

where the dissipator is defined as $\mathcal{D}[A]\rho \equiv A\rho A^\dagger - \frac{1}{2}\{A^\dagger A, \rho\}$. The covariance method then enables the computation of the time evolution for the mean phonon number $\langle b_1^\dagger b_1\rangle(t)$. This is achieved by solving a linear system of differential equations derived within this framework

$$\frac{\mathrm{d}}{\mathrm{d}t}\langle o_i o_j\rangle = \mathrm{Tr}\left(\dot{\rho}\, o_i o_j\right) = \sum_{m,n}\mu_{m,n}\langle o_m o_n\rangle, \tag{14}$$

where o_i, o_j, o_m, o_n denote operators from the set $\{a_1^\dagger, c_1^\dagger, b_1^\dagger, a_1, c_1, b_1\}$, and the coefficients $\mu_{m,n}$ correspond to them. From the master equation, the ordinary differential equations for the second-order moments are derived as follows:

$$\begin{aligned}
\frac{\mathrm{d}}{\mathrm{d}t}\langle a_1^\dagger a_1\rangle =& \ \mathrm{i}g_{ca}\langle c_1^\dagger a_1 - a_1^\dagger c_1\rangle - \kappa_a\langle a_1^\dagger a_1\rangle + \kappa_a\bar{n}_a, \\
\frac{\mathrm{d}}{\mathrm{d}t}\langle c_1^\dagger c_1\rangle =& \ \mathrm{i}g_{ca}\langle a_1^\dagger c_1 - c_1^\dagger a_1\rangle + \mathrm{i}G_{cb}\langle b_1^\dagger c_1 - c_1^\dagger b_1\rangle \\
&+\mathrm{i}G_{cb}\,\mathrm{e}^{-2\mathrm{i}\omega_b t}\langle c_1 b_1\rangle - \mathrm{i}G_{cb}\,\mathrm{e}^{2\mathrm{i}\omega_b t}\langle c_1^\dagger b_1^\dagger\rangle \\
&-\kappa_c\langle c_1^\dagger c_1\rangle + \kappa_c\bar{n}_c, \\
\frac{\mathrm{d}}{\mathrm{d}t}\langle b_1^\dagger b_1\rangle =& -\mathrm{i}G_{cb}\langle b_1^\dagger c_1 - c_1^\dagger b_1\rangle + \mathrm{i}G_{cb}\,\mathrm{e}^{-2\mathrm{i}\omega_b t}\langle c_1 b_1\rangle \\
&-\mathrm{i}G_{cb}\,\mathrm{e}^{2\mathrm{i}\omega_b t}\langle c_1^\dagger b_1^\dagger\rangle - \kappa_b\langle b_1^\dagger b_1\rangle + \kappa_b\bar{n}_b, \\
\frac{\mathrm{d}}{\mathrm{d}t}\langle a_1^\dagger c_1\rangle =& \ \mathrm{i}\delta_a\langle a_1^\dagger c_1\rangle - \mathrm{i}\delta_c\langle a_1^\dagger c_1\rangle + \mathrm{i}g_{ca}\langle c_1^\dagger c_1 - a_1^\dagger a_1\rangle \\
&-\mathrm{i}G_{cb}\langle b_1 a_1^\dagger\rangle - \mathrm{i}G_{cb}\,\mathrm{e}^{2\mathrm{i}\omega_b t}\langle a_1^\dagger b_1^\dagger\rangle \\
&-\frac{1}{2}(\kappa_a+\kappa_c)\langle a_1^\dagger c_1\rangle, \\
\frac{\mathrm{d}}{\mathrm{d}t}\langle a_1^\dagger b_1\rangle =& \ \mathrm{i}\delta_a\langle a_1^\dagger b_1\rangle + \mathrm{i}g_{ca}\langle c_1^\dagger b_1\rangle - \mathrm{i}G_{cb}\langle c_1 a_1^\dagger\rangle \\
&-\mathrm{i}G_{cb}\,\mathrm{e}^{2\mathrm{i}\omega_b t}\langle a_1^\dagger c_1^\dagger\rangle - \frac{1}{2}(\kappa_a+\kappa_b)\langle a_1^\dagger b_1\rangle, \\
\frac{\mathrm{d}}{\mathrm{d}t}\langle c_1^\dagger b_1\rangle =& \ \mathrm{i}\delta_c\langle c_1^\dagger b_1\rangle + \mathrm{i}g_{ca}\langle a_1^\dagger b_1\rangle + \mathrm{i}G_{cb}\langle b_1^\dagger b_1 - c_1^\dagger c_1\rangle \\
&+\mathrm{i}G_{cb}\,\mathrm{e}^{-2\mathrm{i}\omega_b t}\langle b_1 b_1\rangle - \mathrm{i}G_{cb}\,\mathrm{e}^{2\mathrm{i}\omega_b t}\langle c_1^\dagger c_1^\dagger\rangle \\
&-\frac{1}{2}(\kappa_b+\kappa_c)\langle c_1^\dagger b_1\rangle, \\
\frac{\mathrm{d}}{\mathrm{d}t}\langle b_1 b_1\rangle =& -2\mathrm{i}G_{cb}\langle b_1 c_1\rangle - 2\mathrm{i}G_{cb}\,\mathrm{e}^{2\mathrm{i}\omega_b t}\langle c_1^\dagger b_1\rangle - \kappa_b\langle b_1 b_1\rangle, \\
\frac{\mathrm{d}}{\mathrm{d}t}\langle c_1 b_1\rangle =& -\mathrm{i}\delta_c\langle c_1 b_1\rangle - \mathrm{i}G_{cb}\langle c_1 c_1 + b_1 b_1\rangle - \mathrm{i}g_{ca}\langle a_1 b_1\rangle \\
&-\mathrm{i}G_{cb}\,\mathrm{e}^{2\mathrm{i}\omega_b t}\left(\langle c_1^\dagger c_1\rangle + \langle b_1^\dagger b_1\rangle + 1\right) \\
&-\frac{1}{2}(\kappa_b+\kappa_c)\langle c_1 b_1\rangle, \\
\frac{\mathrm{d}}{\mathrm{d}t}\langle a_1^\dagger c_1^\dagger\rangle =& \ \mathrm{i}(\delta_a+\delta_c)\langle a_1^\dagger c_1^\dagger\rangle + \mathrm{i}g_{ca}\langle c_1^\dagger c_1^\dagger + a_1^\dagger a_1^\dagger\rangle + \mathrm{i}G_{cb}\langle a_1^\dagger b_1^\dagger\rangle \\
&+\mathrm{i}G_{cb}\,\mathrm{e}^{-2\mathrm{i}\omega_b t}\langle a_1^\dagger b_1\rangle - \frac{1}{2}(\kappa_c+\kappa_a)\langle a_1^\dagger c_1^\dagger\rangle, \\
\frac{\mathrm{d}}{\mathrm{d}t}\langle a_1^\dagger b_1^\dagger\rangle =& \ \mathrm{i}\delta_a\langle a_1^\dagger b_1^\dagger\rangle + \mathrm{i}g_{ca}\langle c_1^\dagger b_1^\dagger\rangle + \mathrm{i}G_{cb}\langle a_1^\dagger c_1^\dagger\rangle \\
&+\mathrm{i}G_{cb}\,\mathrm{e}^{-2\mathrm{i}\omega_b t}\langle a_1^\dagger c_1 - \frac{1}{2}(\kappa_b+\kappa_a)\langle a_1^\dagger b_1^\dagger\rangle, \\
\frac{\mathrm{d}}{\mathrm{d}t}\langle c_1^\dagger c_1^\dagger\rangle =& \ 2i\delta_c\langle c_1^\dagger c_1^\dagger\rangle + 2\mathrm{i}g_{ca}\langle a_1^\dagger c_1^\dagger\rangle + 2\mathrm{i}G_{cb}\langle b_1^\dagger c_1^\dagger\rangle \\
&+2\mathrm{i}G_{cb}\,\mathrm{e}^{-2\mathrm{i}\omega_b t}\langle c_1^\dagger b_1\rangle - \kappa_c(\bar{n}_c+1)\langle c_1^\dagger c_1^\dagger\rangle \\
&+\kappa_c\bar{n}_c\langle c_1^\dagger c_1^\dagger\rangle, \\
\frac{\mathrm{d}}{\mathrm{d}t}\langle a_1^\dagger a_1^\dagger\rangle =& \ 2i\delta_a\langle a_1^\dagger a_1^\dagger\rangle + 2\mathrm{i}g_{ca}\langle a_1^\dagger c_1^\dagger\rangle \\
&-\kappa_a(\bar{n}_a+1)\langle a_1^\dagger a_1^\dagger\rangle + \kappa_a\bar{n}_a\langle a_1^\dagger a_1^\dagger\rangle.
\end{aligned}$$

The solution of these equations yields the mean values of all time-dependent second-order moments, including $\langle a_1^\dagger a_1\rangle$, $\langle c_1^\dagger c_1\rangle$, $\langle b_1^\dagger b_1\rangle$, $\langle a_1^\dagger c_1\rangle$, $\langle a_1^\dagger b_1\rangle$, $\langle c_1^\dagger b_1\rangle$, $\langle c_1 b_1\rangle$, $\langle a_1^\dagger b_1^\dagger\rangle$, $\langle c_1^\dagger a_1^\dagger\rangle$,

CPB Online In-Press

$\langle b_1^2\rangle$, $\langle c_1^\dagger c_1^\dagger\rangle$, and $\langle a_1^\dagger a_1^\dagger\rangle$. We begin by specifying the initial conditions for the system. The initial conditions are set such that at $t=0$, only the b mode is populated ($\langle b_1^\dagger b_1\rangle \neq 0$), while all other second-order moments are zero. Furthermore, owing to the room-temperature environment, the initial thermal occupation of the optical modes is negligible.

Starting from the initial populations $(N_b, N_a, N_c) = (10^3, 0, 0)$, with $\Omega_0/\omega_b = 0.9$, we compute the evolution of N_b under the CRAB-optimized pulse shown in Fig. 2(b). As displayed in Fig. 3(a), the phonon occupation is suppressed to near the ground state. This result is derived within RWA and neglects all dissipative effects. To account for a realistic system, we introduce dissipation by setting $\kappa_c/\omega_b = 0.5$, $\kappa_a/\omega_b = 2$, and a mechanical quality factor $Q_b = \omega_b/\kappa_b = 10^7$; the resulting dynamics are plotted in Fig. 3(b). As in the closed system, the phonon occupation is again reduced almost to the ground state. When the counter-rotating terms are considered, the mechanical occupation exhibits pronounced fluctuations when the pulse reaches its local maximum. However, the mechanical mode is eventually cooled to the ground state. Furthermore, as demonstrated in Fig. 4, the CRAB method remains effective across a wide parameter range, extending from the conventional resolved-sideband regime to strong coupling and unresolved-sideband conditions.

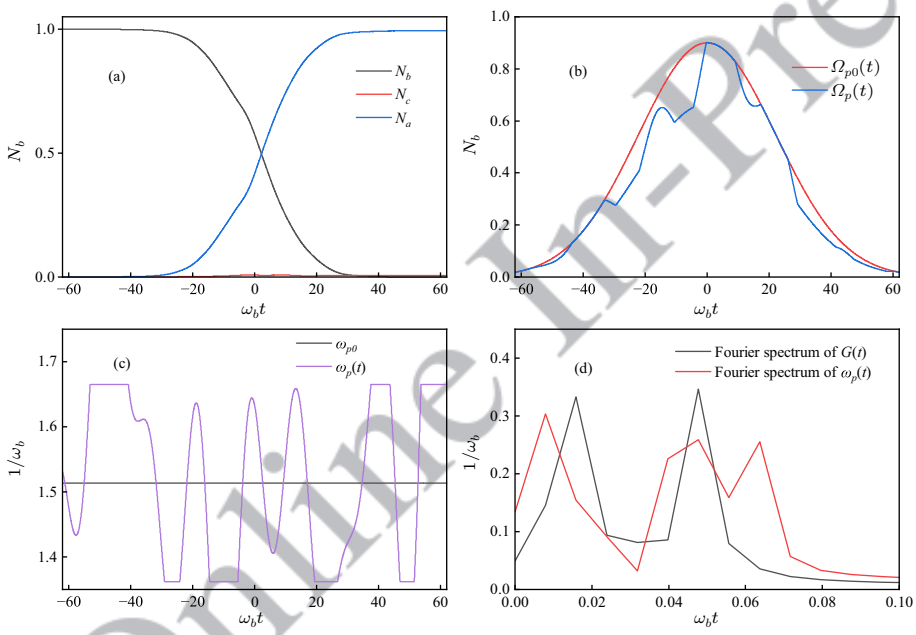


Fig. 2. (a) Unitary time evolution of the modal populations under the pulses shown in (b). Here, N_b, N_a, and N_c denote the populations of the mechanical mode, primary cavity mode, and auxiliary cavity mode, respectively, starting from $(N_b, N_c, N_a) = (1, 0, 0)$. (b) Hypothetical Gaussian pulse $\Omega_{p_0}(t)$ and its CRAB-optimized version $\Omega_p(t)$, $\Omega_0 = 0.9$. (c) Optimized ω_{p_0} and the time-dependent modulated frequency $\omega_p(t)$, both in units of ω_b. (d) Normalized amplitude spectra of $G(t)$ and $F(t)$, the frequency is in units of ω_b.

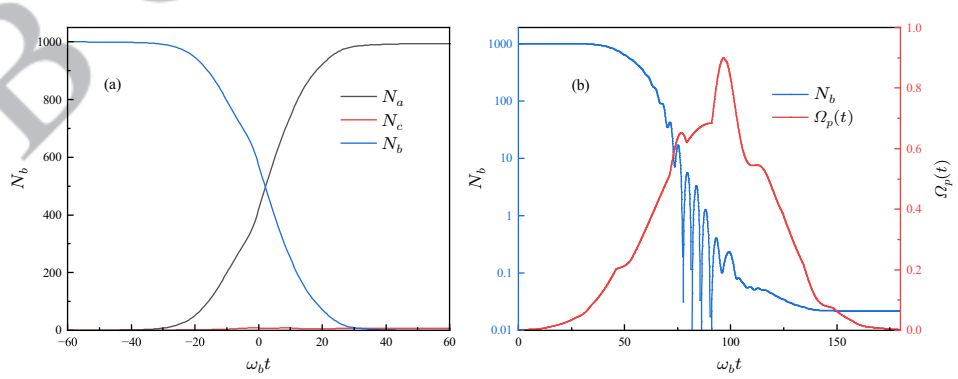


Fig. 3. Phonon cooling in closed and open quantum systems. (a) Evolution of mode occupations in closed system under the CRAB-optimized pulse, with initial condition $(N_b, N_a, N_c) = (10^3, 0, 0)$. The dynamics are obtained by solving the master equation within RWA. (b) Mode occupations beyond the RWA in open system with $(\kappa_c, \kappa_a)/\omega_b = (0.5, 2.0)$, and $Q_b = 10^7$.

3.3. Cooling mechanism

The physical cooling mechanism is illustrated in Fig. 5. The frequency modulation keeps the detuning positive ($\delta_c > 0$) throughout the pulse, as shown in Fig. 5(a). This persistent red-detuned configuration favors anti-Stokes scattering, which pumps energy from the mechanical mode into the optical cavity.

The amplitude modulation simultaneously opens a transfer window. Phonons flow into the primary cavity and are

CPB Online in-Press

quickly dissipated by its intrinsic decay κ_c. The auxiliary cavity provides an extra drain via the coupling g_{ca}. Although its occupation N_a remains low (Fig. 5(a)), it carries away about 37% of the total dissipated energy (Fig. 5(c)) and accelerates the cooling. A comparison with the case $g_{ca} = 0$ (Fig. 5(b)) confirms that the auxiliary cavity shortens the cooling time, even though the final phonon number hardly changes (from $N_{\min} = 0.022$ to 0.031).

In the ideal closed-system limit without cavity dissipation, the optimized pulses would realize a STIRAP-like dark-state transfer. This process moves the mechanical excitation to the auxiliary cavity without populating the primary cavity. Under the practical parameters considered here, the cavity decay rates are non-negligible. The CRAB optimizer therefore finds a more efficient route, a red-detuned transfer combined with rapid optical dissipation. This hybrid strategy achieves ground-state cooling across the full parameter range without any pre-programmed pulse sequence.

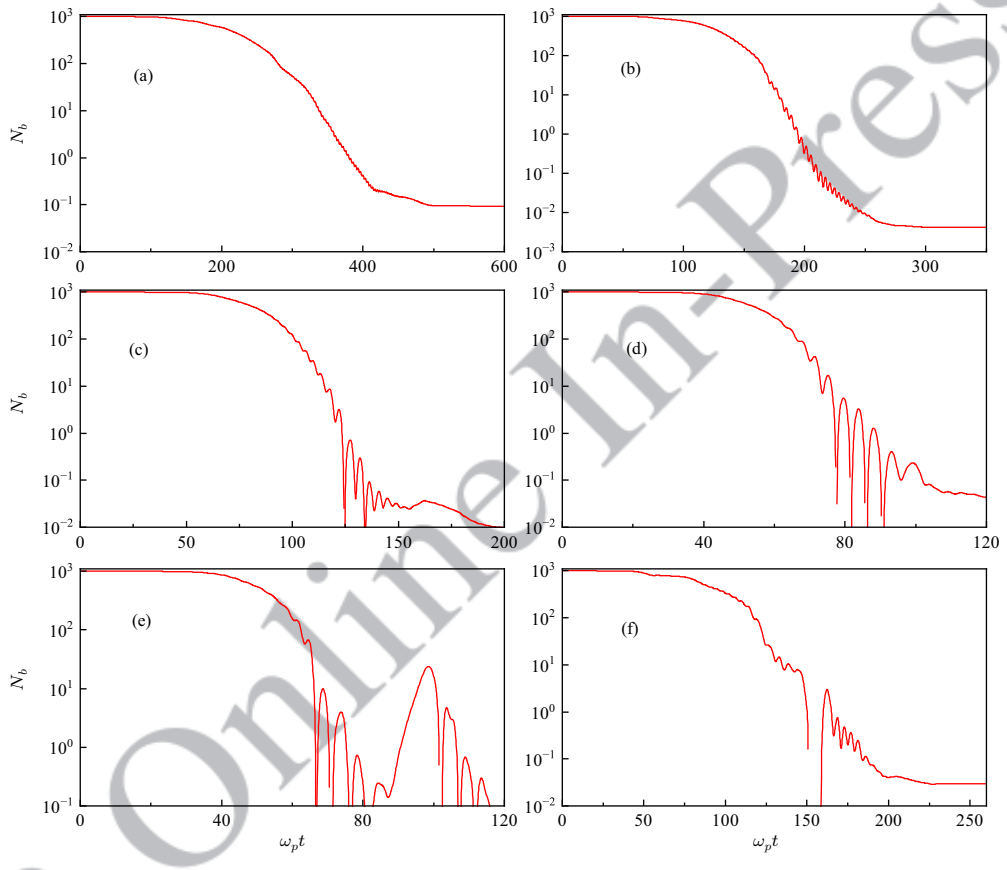


Fig. 4. Phonon cooling in an open quantum system under different conditions, corresponding to the cases in Table 1: No. 12 (a), No. 16 (b), No. 20 (c), No. 24 (d), No. 28 (e), and No. 32 (f).

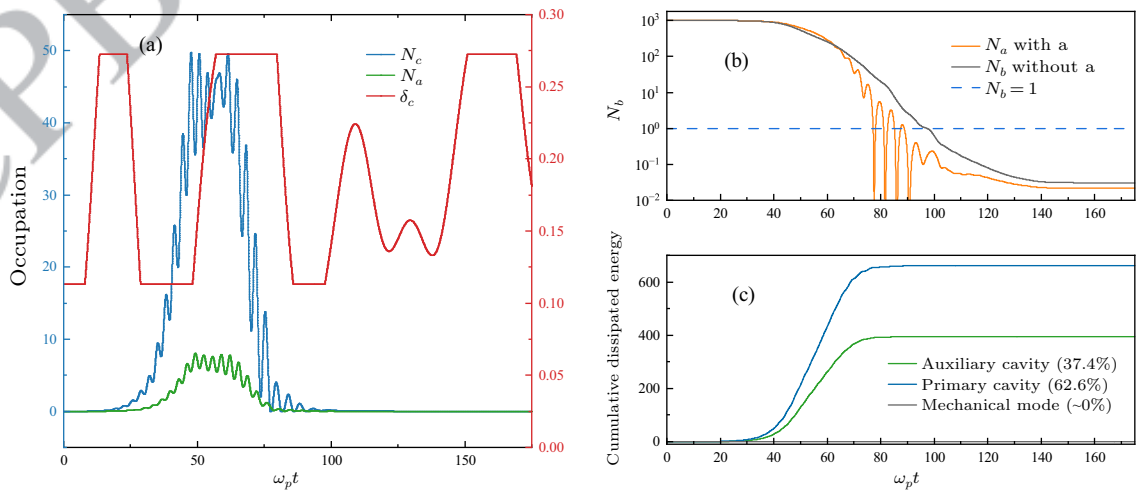


Fig. 5. Red-detuned cooling dynamics with auxiliary cavity acceleration, obtained with the same parameters as Fig. 3. (a) Cavity occupations N_c, N_a and the detuning δ_c versus time, showing that the system is consistently maintained in the red-detuned regime ($\delta_c > 0$). (b) Mechanical occupation N_b with and without the auxiliary cavity, demonstrating the acceleration of cooling by the additional dissipation channel. (c) Cumulative dissipated energy distribution among the three modes.

CPB Online In-Press

Table 1. Final-time phonon number $N_{\min}$ (instantaneous value at the end of the pulse), maximum noise standard deviations $\sigma_w^{\max}$ (white noise) and $\sigma_h^{\max}$ (pulse distortion), and Gaussian pulse width parameter τ. The cooling contraction factor $\lambda_b = \|\boldsymbol{P}_b\boldsymbol{\Phi}(T,0)\|_{\mathrm{F}}$ (defined in Eq. (18)) and the rigorous upper bound $N_{\mathrm{bound}} = \frac{1}{2}\left[(N_b+\frac{1}{2})\lambda_b^2 + 2\varepsilon - 1\right]$ are listed in the last two columns. For a few parameter sets, N_{bound} is marginally lower than $N_{\min}$ by ≤ 0.002, which is within the numerical tolerance of the adjoint integration. For No. 29, the adjoint system did not fully converge due to extreme stiffness, the corresponding N_{bound} entries are therefore omitted.

No.	Ω_0/ω_b	κ_c/ω_b	κ_a/ω_b	Q_b	$N_{\min}$	$\sigma_w^{\max}$	$\sigma_h^{\max}$	τ	λ_b	N_{bound}
1	0.02	0.05	0.01	10^5	0.421	>0.5	0.165	507.50	0.029	0.421
2	0.02	0.05	2	10^5	0.437	>0.5	0.113	507.50	0.030	0.437
3	0.02	0.05	0.01	10^7	0.468	>0.5	0.122	507.50	0.031	0.468
4	0.02	0.05	2	10^7	0.512	>0.5	>0.2	507.50	0.032	0.512
5	0.1	0.1	0.01	10^5	0.004	>0.5	0.097	181.25	0.003	0.004
6	0.1	0.1	2	10^5	0.002	>0.5	0.156	181.25	0.002	0.002
7	0.1	0.1	0.01	10^7	0.462	>0.5	>0.2	181.25	0.030	0.461
8	0.1	0.1	2	10^7	0.001	0.224	>0.2	181.25	0.001	0.001
9	0.3	0.1	0.01	10^5	0.599	>0.5	0.091	163.12	0.035	0.600
10	0.3	0.1	2	10^5	0.467	>0.5	>0.2	126.88	0.031	0.475
11	0.3	0.1	0.01	10^7	0.319	0.267	0.032	163.12	0.025	0.318
12	0.3	0.1	2	10^7	0.093	>0.5	0.151	126.88	0.014	0.100
13	0.5	0.2	0.01	10^5	0.008	0.353	0.046	108.75	0.002	0.007
14	0.5	0.2	2	10^5	0.004	>0.5	0.124	72.50	0.000	0.005
15	0.5	0.2	0.01	10^7	0.004	0.354	0.113	108.75	0.087	3.789
16	0.5	0.2	2	10^7	0.004	>0.5	0.175	72.50	0.000	0.006
17	0.6	0.3	0.01	10^5	0.019	0.424	0.122	72.50	0.004	0.018
18	0.6	0.3	2	10^5	0.008	0.437	>0.2	54.38	0.000	0.012
19	0.6	0.3	0.01	10^7	0.008	>0.5	0.133	54.38	0.003	0.021
20	0.6	0.3	2	10^7	0.008	>0.5	>0.2	54.38	0.000	0.012
21	0.9	0.5	0.01	10^5	0.021	0.477	0.057	54.38	0.001	0.021
22	0.9	0.5	2	10^5	0.022	>0.5	>0.2	36.25	0.000	0.031
23	0.9	0.5	0.01	10^7	0.019	0.461	0.074	54.38	0.001	0.018
24	0.9	0.5	2	10^7	0.022	>0.5	>0.2	36.25	0.000	0.030
25	1.2	0.5	0.01	10^5	0.008	0.200	0.088	108.75	0.000	0.010
26	1.2	0.5	2	10^5	0.021	>0.5	0.141	36.25	0.000	0.036
27	1.2	0.5	0.01	10^7	0.008	0.175	0.132	108.75	0.000	0.010
28	1.2	0.5	2	10^7	0.021	>0.5	0.113	36.25	0.000	0.035
29	1.5	0.5	0.01	10^5	0.563	0.197	0.034	54.38	0.027	—
30	1.5	0.5	2	10^5	0.021	0.219	0.028	54.38	0.002	0.025
31	1.5	0.5	0.01	10^7	0.024	0.256	0.031	54.38	0.001	0.022
32	1.5	0.5	2	10^7	0.029	0.004	0.001	54.38	0.038	1.191
33	0.2	4	0.01	10^5	0.948	>0.5	>0.2	906.25	0.023	0.957
34	0.2	4	2	10^5	0.935	>0.5	>0.2	906.25	0.022	0.942
35	0.2	4	0.01	10^7	0.977	>0.5	>0.2	906.25	0.024	0.986
36	0.2	4	2	10^7	0.955	>0.5	>0.2	906.25	0.023	0.962
37	0.5	10	0.01	10^5	2.991	>0.5	>0.2	906.25	0.024	3.218
38	0.5	10	2	10^5	2.806	>0.5	>0.2	906.25	0.017	2.857
39	0.5	10	0.01	10^7	2.842	>0.5	>0.2	906.25	0.020	3.016
40	0.5	10	2	10^7	2.289	>0.5	>0.2	906.25	0.018	2.331

3.4. Robustness

In a realistic experimental setting, various non-ideal factors will influence the system's evolution. In our model, we specifically account for noise arising from the control signals and distortions in their spectral profiles. As a tractable approximation for the dominant stochastic technical noise, such as laser amplitude/phase noise and electronic noise, we introduce additive Gaussian white noise to the ideal control signals. The fundamental quantum noise of the system is inherently included in our model through the dissipation rates and the associated input quantum fields of the optical and mechanical modes.

To assess experimental robustness, we consider two sources of imperfection, additive Gaussian white noise on the control signals and spectral distortion of the optimized pulse shape. For each type, we fix the imperfection strength σ and perform 30 independent trials with different random realizations of the noise or distortion waveform. The protocol is considered robust under imperfection strength σ if, for all 30 trials, the following conditions are met: final occupations satisfy $\langle N_b\rangle < 0.01N_b^0$, $\langle N_a\rangle < 0.005N_b^0$, $\langle N_c\rangle < 0.005N_b^0$. The maximum transient populations satisfy $\max_t\langle N_a(t)\rangle < 0.1N_b^0$ and $\max_t\langle N_c(t)\rangle < 0.1N_b^0$, where $N_b^0 = 10^3$ is the initial phonon occupation.

We add Gaussian white noise $\Delta_\Omega^{\mathrm{noise}}(t)$ and $\Delta_\omega^{\mathrm{noise}}(t)$ to the control signals, with standard deviations $\Omega_0\sigma_w$ and $\omega_p^{\max}\sigma_w$, respectively. Here, $\omega_p^{\max}$ is the maximum of $\omega_p(t)$, and σ_w is a normalized noise strength parameter quantifying the relative magnitude of fluctuations. The noisy control signals are then given by

$$\begin{aligned}\Omega_p^{\mathrm{noise}}(t) &= \Omega_p(t) + \Delta_\Omega^{\mathrm{noise}}(t),\\ \omega_p^{\mathrm{noise}}(t) &= \omega_p(t) + \Delta_\omega^{\mathrm{noise}}(t).\end{aligned} \tag{15}$$

We determine the maximum tolerable relative noise intensity $\sigma_w^{\max}$ via a binary search: starting with $\sigma_{\mathrm{low}} = 10^{-6}$ and an initial $\sigma_{\mathrm{high}} = 0.5$, we first verify that the robustness criterion is satisfied at σ_{low}; otherwise, no solution exists. If the criterion is also satisfied at σ_{high}, we establish an interval $[\sigma_{\mathrm{low}}, \sigma_{\mathrm{high}}]$. We then iteratively evaluate the midpoint $\sigma_{\mathrm{mid}} = (\sigma_{\mathrm{low}} + \sigma_{\mathrm{high}})/2$ by running 30 independent noise realizations at this noise level. Depending on whether the cooling criterion is met, we update $\sigma_{\mathrm{low}} \leftarrow \sigma_{\mathrm{mid}}$ or $\sigma_{\mathrm{high}} \leftarrow \sigma_{\mathrm{mid}}$. This process is repeated until the relative interval width $(\sigma_{\mathrm{high}} - \sigma_{\mathrm{low}})/\sigma_{\mathrm{low}}$ falls below a tolerance $\varepsilon = 10^{-3}$ or a maximum of 25 iterations is reached. The final σ_{low} is taken as $\sigma_w^{\max}$. Since a relative noise intensity $\sigma_w > 0.5$ would artificially enhance the cooling, we cap the search at 0.5 and record any such outcome as $\sigma_w^{\max} > 0.5$.

We perturb the optimized Fourier coefficients a_k, d_k by adding zero-mean Gaussian noise with standard deviation σ_h, generating distorted pulses via

$$\begin{aligned}\Omega_p^{\mathrm{dist}}(t) &= \Omega_{p_0}(t)\Big[1 + 0.5\sum_{k=1}^{N}(a_k + \Delta_k^\Omega)g_k(\omega_k t)\Big],\\ \omega_p^{\mathrm{dist}}(t) &= \omega_{p_0}\Big[1 + 0.2\sum_{k=1}^{N}(d_k + \Delta_k^\omega)g_k(\omega_k t)\Big],\end{aligned} \tag{16}$$

where $g_k(\omega_k t)$ are sinusoidal basis functions (e.g., sin and cos), and $\Delta_k^\Omega, \Delta_k^\omega \sim \mathcal{N}(0, \sigma_h^2)$ are independent for each k and between the two series. The maximum tolerable $\sigma_h^{\max}$ is then

CPB Online First

determined by the same binary search procedure as in the additive white noise case, requiring all 30 noise realizations to satisfy the robustness conditions. If the found maximum exceeds 0.2, we record $\sigma_h^{\max} > 0.2$.

As shown in Fig. 6, the CRAB method exhibits excellent robustness against white noise and pulse distortion. Even when the relative strength of the white noise reaches 0.5 (Fig. 7(a)), the phonon occupation is still reduced to the ground state. Counterintuitively, the addition of white noise accelerates the phonon cooling compared to the noiseless case — a behavior that may stem from noise-assisted escape from local minima in the CRAB-optimized control landscape, or from an effectively enhanced dissipation rate caused by the broadened frequency spectrum of the noisy pulse.

The method is also robust against pulse distortion, as illustrated in Fig. 7(c): although the pulse amplitude can be significantly distorted, the mechanical mode is still cooled to nearly the ground state. As indicated by the yellow shaded band in Fig. 6, even though the incorporation of pulse distortion introduces pronounced fluctuations in the cooling dynamics, the phonon occupation at the final time still reaches the ground state, similar to the noiseless case.

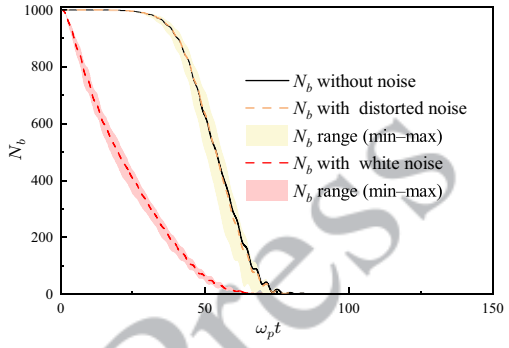


Fig. 6. Evolution of mode occupations for phonon cooling under three conditions: noiseless, white noise, and a distorted pulse. For the noisy cases, dash lines represent the ensemble mean over 30 independent realizations, and the shaded bands indicate the corresponding min–max range. Parameters are taken from Table 1, No. 24.

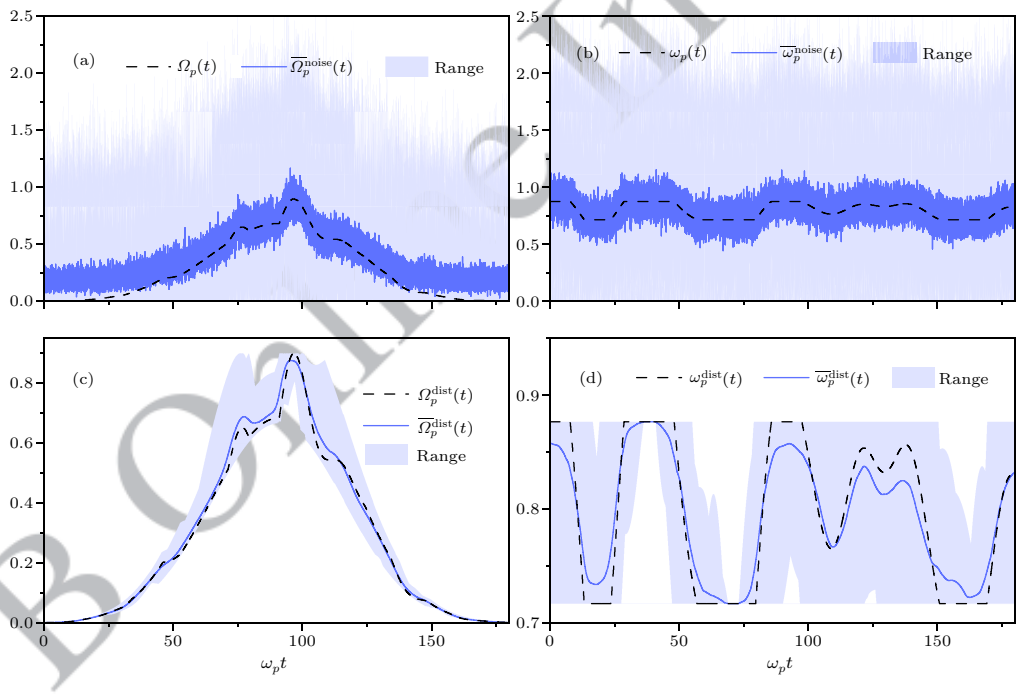


Fig. 7. (a) and (b) White-noise model. (c) and (d) CRAB-distortion noise model. (a) and (c) Amplitude $\Omega_p(t)$. (b) and (d) Frequency $\omega_p(t)$. Dashed black: noiseless CRAB-optimized pulse/frequency. Solid line: ensemble mean ($\overline{\Omega}_p^{\rm noise}(t)$, $\overline{\omega}_p^{\rm noise}(t)$, $\overline{\Omega}_p^{\rm dist}(t)$ or $\overline{\omega}_p^{\rm dist}(t)$) over 30 realizations. Shaded band: min–max envelope of the trajectories.

4. Stability analysis and comparison with conventional methods

In standard continuous-wave optomechanical sideband cooling, the linearized dynamics around the steady state is governed by a set of Langevin equations. The stability of this steady state can be analyzed via the Routh–Hurwitz (RH) criterion, which for our tripartite system (primary cavity, auxiliary cavity, and mechanical mode) yields a necessary and sufficient condition for asymptotic stability. Following the standard procedure,[32] the dominant stability condition reduces to

$$|G_{cb}|^2 < \frac{\omega_b^2}{4} + \frac{\kappa_c^2}{16}. \tag{17}$$

If this inequality is violated, the system develops a parametric instability: the mechanical mode and the cavity fields enter a self-sustained oscillatory regime where phonon number grows exponentially until limited by nonlinearities, making ground-state cooling impossible.

In our scheme, the driving amplitude and frequency are actively modulated, making the linearized system matrix

CPB Online First Press

$\boldsymbol{M}(t)$ explicitly time-dependent. Consequently, the conventional Routh–Hurwitz criterion, which is designed for time-invariant matrices, is no longer applicable. To analyze the stability of this time-varying dynamics, we introduce the state transition matrix $\boldsymbol{\Phi}(t,\tau)$ and the associated cooling contraction factor

$$\lambda_b \equiv \|\boldsymbol{P}_b \boldsymbol{\Phi}(T,0)\|_{\mathrm{F}}, \tag{18}$$

where $\boldsymbol{P}_b$ projects onto the mechanical mode. A rigorous proof given in Appendix A5 shows that if the optimized pulse yields $\lambda_b < 1$, the final phonon number satisfies the approximate upper bound

$$\langle b_1^\dagger b_1 \rangle(T) \lesssim \frac{1}{2} N_b \lambda_b^2 + \varepsilon, \tag{19}$$

where N_b is the initial thermal occupation and ε accounts for the accumulated quantum noise. The conditions $\lambda_b \ll 1$ and $\varepsilon < 1$ are sufficient for ground-state cooling. As shown in Table 1, all CRAB-optimized pulses indeed yield λ_b on the order of 10^{-2}–10^{-6}, firmly satisfying $\lambda_b \ll 1$. The corresponding upper bounds N_{bound} are listed alongside N_{min}; for the vast majority of cases $N_{\mathrm{min}} \leq N_{\mathrm{bound}}$ holds as required. In a few instances, the bound lies marginally below the simulated value by ≤ 0.002, which is within the numerical tolerance of the adjoint integration for stiff dynamics. For one parameter set (No. 29), the adjoint integration did not fully converge; the corresponding bound is therefore omitted in the table.

We now examine the parameters listed in Table 1, Nos. 17–32. According to the Routh–Hurwitz criterion, conventional continuous-wave sideband cooling would be unconditionally unstable for all these parameters.[33] In stark contrast, our CRAB-based pulsed cooling scheme does not rely on a stationary equilibrium point. Thus, our method achieves stable and efficient cooling across the entire parameter range Nos. 17–32. The final phonon numbers N_{min} reported in Table 1 (e.g., 0.022 for No. 24, 0.021 for No. 28, 0.029 for No. 32) all lie well below unity, and no divergence is observed in the time evolution (see Figs. 4(c)–4(f)). Although self-oscillations become more pronounced as the driving amplitude Ω_0 (which sets the strength of the full optomechanical coupling, including the instability-inducing counter-rotating terms) increases, the mechanical mode can still be cooled to the ground state. Moreover, even for parameter sets where conventional cooling does satisfy the stability criterion (e.g., Nos. 13–16 and Nos. 33–40, corresponding to the resolved-sideband and unresolved-sideband regimes respectively), our scheme still outperforms standard cooling.

5. Conclusion

We have numerically demonstrated an efficient cooling protocol for an optomechanical system where a mechanical mode is strongly coupled to two optical modes. By optimizing the amplitude and frequency of a single drive field with CRAB, we modulate the coupling rate $G_{cb}(t)$ and the detunings $\delta_a(t)$, $\delta_c(t)$, thereby achieving near-unity transfer efficiency over a wide parameter range, including the strong-coupling and unresolved-sideband regimes where conventional methods fail.

We have clarified the underlying cooling mechanism. The frequency modulation maintains a persistent red-detuned regime ($\delta_c > 0$), ensuring preferential anti-Stokes scattering that directs energy from the mechanical mode to the optical modes. The primary cavity's intrinsic decay κ_c provides the dominant dissipation channel, while the auxiliary cavity acts as an accelerator that significantly shortens the cooling time without requiring high population. In the ideal closed-system limit, the optimized pulses would realize a STIRAP-like dark-state transfer; under practical parameters, the CRAB optimizer automatically discovers the more efficient red-detuned direct-dissipation route.

A central result of this work is a rigorous finite-time contraction theorem (proved in Appendix A5) that guarantees ground-state cooling whenever the cooling contraction factor λ_b is smaller than unity. The theorem provides an exact upper bound on the final phonon number, $N_{\mathrm{bound}} = \frac{1}{2}[(N_b + \frac{1}{2})\lambda_b^2 + 2\varepsilon - 1]$, which is satisfied by the vast majority of parameter sets listed in Table 1. The computed λ_b values are on the order of 10^{-2}–10^{-6}, confirming that the CRAB-optimized pulses are strongly contractive and that the stability condition is robustly fulfilled. Furthermore, the optimized pulses exhibit strong robustness against experimental imperfections: cooling remains effective under additive Gaussian white noise and spectral distortions, demonstrating that the contraction property is structurally stable and not sensitive to fine-tuned waveforms. The combination of a rigorous stability proof, comprehensive numerical verification, and excellent robustness makes our scheme a promising candidate for ground-state cooling in on-chip optomechanical devices, where only a single modulated drive is required.

Appendix A: Strict proof of the finite-time contraction theorem

In this appendix, we provide a rigorous proof of the finite-time contraction theorem stated in Section 4. We retain the full counter-rotating terms in the linearized Hamiltonian and explicitly account for both thermal and vacuum noise. All symbols follow the definitions in the main text.

CPB Online In Press

A1. Linearized quantum Langevin equation in orthogonal quadratures

The linearized Hamiltonian in the interaction picture is given by Eq. (8) of the main text:

$$\begin{aligned} H \;=\; & \delta_a(t)\, a_1^\dagger a_1 + \delta_c(t)\, c_1^\dagger c_1 + G_{cb}(t)\big(c_1^\dagger b_1 + c_1 b_1^\dagger\big) \\ & + G_{cb}(t)\big(\mathrm{e}^{-2\mathrm{i}\omega_b t} c_1 b_1 + \mathrm{e}^{2\mathrm{i}\omega_b t} c_1^\dagger b_1^\dagger\big) \\ & + g_{ca}\big(c_1^\dagger a_1 + a_1^\dagger c_1\big), \end{aligned} \tag{A1}$$

where $\delta_a(t) = \omega_a - \omega_b - \omega_p(t)$, $\delta_c(t) = \omega_c - \omega_b - \omega_p(t)$, and $G_{cb}(t) = \eta(t)\, g_{cb}$ is the linearized optomechanical coupling. The operators a_1, b_1, c_1 are the fluctuation operators of the auxiliary cavity, mechanical, and primary cavity modes, respectively.

Define the dimensionless quadrature operators

$$\hat{X}_k = \frac{k + k^\dagger}{\sqrt{2}}, \quad \hat{Y}_k = \frac{k - k^\dagger}{i\sqrt{2}}, \quad k = b, c, a, \tag{A2}$$

which satisfy $[\hat{X}_k, \hat{Y}_l] = \mathrm{i}\,\delta_{kl}$. Collecting them into a vector $\hat{\boldsymbol{R}} = (\hat{X}_b, \hat{Y}_b, \hat{X}_c, \hat{Y}_c, \hat{X}_a, \hat{Y}_a)^\top$, the full linearized quantum Langevin equations (including dissipation and noise) can be written as

$$\frac{\mathrm{d}}{\mathrm{d}t}\hat{\boldsymbol{R}}(t) = \boldsymbol{M}(t)\,\hat{\boldsymbol{R}}(t) + \hat{\boldsymbol{N}}(t). \tag{A3}$$

The time-dependent 6×6 matrix $\boldsymbol{M}(t)$ is obtained by projecting the Heisenberg-Langevin equations onto the quadrature basis. With all counter-rotating terms kept, its explicit form is

$$\boldsymbol{M}(t) = \begin{pmatrix} -\frac{\kappa_b}{2} & 0 & Gs & G(1-c) & 0 & 0 \\ 0 & -\frac{\kappa_b}{2} & -G(1+c) & -Gs & 0 & 0 \\ Gs & G(1-c) & -\frac{\kappa_c}{2} & \delta_c & 0 & g \\ -G(1+c) & -Gs & -\delta_c & -\frac{\kappa_c}{2} & -g & 0 \\ 0 & 0 & 0 & g & -\frac{\kappa_a}{2} & \delta_a \\ 0 & 0 & -g & 0 & -\delta_a & -\frac{\kappa_a}{2} \end{pmatrix}, \tag{A4}$$

where $G \equiv G_{cb}(t)$, $g \equiv g_{ca}$, $c = \cos(2\omega_b t)$, $s = \sin(2\omega_b t)$, and $\delta_a(t) = \omega_a - \omega_b - \omega_p(t)$, $\delta_c(t) = \omega_c - \omega_b - \omega_p(t)$. The rows and columns correspond to the quadrature operators $(X_b, Y_b, X_c, Y_c, X_a, Y_a)$ in this order. The noise vector $\hat{\boldsymbol{N}}(t)$ has zero mean and white-noise correlations

$$\langle \hat{N}_j(t) \hat{N}_k(t') \rangle = \boldsymbol{D}_{jk}\, \delta(t - t'), \tag{A5}$$

with the constant diffusion matrix

$$\begin{aligned} \boldsymbol{D} \;=\; & \mathrm{diag}\Big(\kappa_b(\bar{n}_b + \tfrac{1}{2}),\, \kappa_b(\bar{n}_b + \tfrac{1}{2}),\, \kappa_c(\bar{n}_c + \tfrac{1}{2}), \\ & \kappa_c(\bar{n}_c + \tfrac{1}{2}),\, \kappa_a(\bar{n}_a + \tfrac{1}{2}),\, \kappa_a(\bar{n}_a + \tfrac{1}{2})\Big). \end{aligned} \tag{A6}$$

At the cryogenic temperatures considered in the main text, $\bar{n}_a, \bar{n}_c \approx 0$ and $\bar{n}_b \ll 1$, but the quantum vacuum terms $\frac{1}{2}$ are always present.

A2. Covariance matrix and time-dependent Lyapunov equation

Because the Hamiltonian is bilinear and the noise is Gaussian, the state remains Gaussian at all times. All second-order statistics are encoded in the covariance matrix

$$\boldsymbol{V}(t) = \frac{1}{2}\langle \{\hat{\boldsymbol{R}}(t), \hat{\boldsymbol{R}}^\top(t)\} \rangle - \langle \hat{\boldsymbol{R}}(t) \rangle \langle \hat{\boldsymbol{R}}(t) \rangle^\top. \tag{A7}$$

The mean values vanish for the initial thermal state and the zero-mean noise, so $\boldsymbol{V}(t) = \frac{1}{2}\langle \{\hat{\boldsymbol{R}}, \hat{\boldsymbol{R}}^\top\} \rangle$. Applying the Ito rule to Eq. (A3) yields the deterministic time-dependent Lyapunov equation

$$\frac{\mathrm{d}}{\mathrm{d}t}\boldsymbol{V}(t) = \boldsymbol{M}(t)\boldsymbol{V}(t) + \boldsymbol{V}(t)\boldsymbol{M}^\top(t) + \boldsymbol{D}. \tag{A8}$$

The initial condition corresponds to a thermal mechanical mode and vacuum optical modes,

$$\boldsymbol{V}(0) = \mathrm{diag}\big(N_b + \tfrac{1}{2}, N_b + \tfrac{1}{2}, \tfrac{1}{2}, \tfrac{1}{2}, \tfrac{1}{2}, \tfrac{1}{2}\big), \tag{A9}$$

with $N_b = \langle b_1^\dagger b_1 \rangle_{t=0} \gg 1$.

The phonon number is obtained from the first two diagonal entries of $\boldsymbol{V}(t)$ as

$$\langle b_1^\dagger b_1 \rangle(t) = \frac{1}{2}\big(V_{11}(t) + V_{22}(t) - 1\big). \tag{A10}$$

A3. State transition matrix and explicit solution

We define the state transition matrix $\boldsymbol{\Phi}(t, \tau)$ as the solution of the homogeneous equation

$$\frac{\mathrm{d}}{\mathrm{d}t}\boldsymbol{\Phi}(t, \tau) = \boldsymbol{M}(t)\boldsymbol{\Phi}(t, \tau), \qquad \boldsymbol{\Phi}(\tau, \tau) = \boldsymbol{I}_6. \tag{A11}$$

It satisfies the group property $\boldsymbol{\Phi}(t, s)\boldsymbol{\Phi}(s, \tau) = \boldsymbol{\Phi}(t, \tau)$. By the variation-of-constants formula, the solution of Eq. (A8) is

$$\boldsymbol{V}(t) = \boldsymbol{\Phi}(t, 0)\boldsymbol{V}(0)\boldsymbol{\Phi}^\top(t, 0) + \int_0^t \boldsymbol{\Phi}(t, s)\, \boldsymbol{D}\, \boldsymbol{\Phi}^\top(t, s)\, \mathrm{d}s. \tag{A12}$$

CPB Online In-Press

The first term represents the residual of the initial thermal excitation after the pulse, while the second term is the cumulative contribution of all quantum noise injected during $[0,t]$.

A4. Upper bound on the final mechanical occupation

Let T be the pulse duration. Introduce the projection onto the mechanical subspace, $\boldsymbol{P}_b = \mathrm{diag}(1,1,0,0,0,0)$. From Eqs. (A12) and (A10) we have

$$\begin{aligned}\langle b_1^\dagger b_1\rangle(T) &= \frac{1}{2}\mathrm{Tr}\big[\boldsymbol{P}_b\boldsymbol{V}(T)\boldsymbol{P}_b\big]-\frac{1}{2}\\ &= \frac{1}{2}\mathrm{Tr}\big[\boldsymbol{P}_b\boldsymbol{\Phi}(T,0)\boldsymbol{V}(0)\boldsymbol{\Phi}^\top(T,0)\boldsymbol{P}_b\big]\\ &\quad+\frac{1}{2}\int_0^T \mathrm{Tr}\big[\boldsymbol{P}_b\boldsymbol{\Phi}(T,s)\boldsymbol{D}\boldsymbol{\Phi}^\top(T,s)\boldsymbol{P}_b\big]\,\mathrm{d}s\\ &\quad-\frac{1}{2}. \end{aligned}\tag{A13}$$

Define $\boldsymbol{W}\equiv\boldsymbol{P}_b\boldsymbol{\Phi}(T,0)$, a 2×6 matrix. Using the trace inequality $\mathrm{Tr}[\boldsymbol{W}\boldsymbol{V}(0)\boldsymbol{W}^\top]\le\|\boldsymbol{V}(0)\|\,\|\boldsymbol{W}\|_{\mathrm{F}}^2$, where $\|\cdot\|$ is the spectral norm and $\|\cdot\|_{\mathrm{F}}$ the Frobenius norm, and noting $\|\boldsymbol{V}(0)\|=N_b+\frac{1}{2}$ from (A9), we obtain

$$\begin{aligned}&\mathrm{Tr}\big[\boldsymbol{P}_b\boldsymbol{\Phi}(T,0)\boldsymbol{V}(0)\boldsymbol{\Phi}^\top(T,0)\boldsymbol{P}_b\big]\\ &\le (N_b+\tfrac{1}{2})\,\|\boldsymbol{P}_b\boldsymbol{\Phi}(T,0)\|_{\mathrm{F}}^2.\end{aligned}\tag{A14}$$

We introduce the cooling contraction factor

$$\lambda_b\equiv\|\boldsymbol{P}_b\boldsymbol{\Phi}(T,0)\|_{\mathrm{F}}=\sqrt{\sum_{j=1}^{2}\sum_{k=1}^{6}\big|[\boldsymbol{\Phi}(T,0)]_{jk}\big|^2}.\tag{A15}$$

The first term in (A13) is therefore bounded by $(N_b+\frac{1}{2})\lambda_b^2$.

The noise integral is denoted by

$$\varepsilon\equiv\frac{1}{2}\int_0^T\mathrm{Tr}\big[\boldsymbol{P}_b\boldsymbol{\Phi}(T,s)\boldsymbol{D}\boldsymbol{\Phi}^\top(T,s)\boldsymbol{P}_b\big]\,\mathrm{d}s,\tag{A16}$$

which is a finite constant that depends only on the bath parameters and the pulse shape. At cryogenic temperatures, ε is finite and its value depends on the specific system parameters and the optimized pulse shape.

Combining the two estimates, we arrive at the rigorous upper bound

$$\langle b_1^\dagger b_1\rangle(T)\le\frac{1}{2}\Big[(N_b+\tfrac{1}{2})\lambda_b^2+2\varepsilon-1\Big].\tag{A17}$$

A5. Finite-time contraction theorem and stability

From (A17) we immediately deduce the following theorem: **Theorem 1 (Finite-time contraction stability)**. Consider the time-dependent linear system described by the matrix $\boldsymbol{M}(t)$ given in Eq. (A4) driven by the optimized CRAB pulses $\Omega_p(t),\omega_p(t)$. Let $\lambda_b=\|\boldsymbol{P}_b\boldsymbol{\Phi}(T,0)\|_{\mathrm{F}}$ and $\varepsilon=\frac{1}{2}\int_0^T\mathrm{Tr}[\boldsymbol{P}_b\boldsymbol{\Phi}(T,s)\boldsymbol{D}\boldsymbol{\Phi}^\top(T,s)\boldsymbol{P}_b]\mathrm{d}s$. If $\lambda_b<1$, then for any initial thermal phonon number N_b, the final phonon number satisfies the strict upper bound

$$\langle b_1^\dagger b_1\rangle(T)\le\frac{1}{2}\Big[(N_b+\tfrac{1}{2})\lambda_b^2+2\varepsilon-1\Big].$$

Ground-state cooling ($\langle b_1^\dagger b_1\rangle(T)<1$) is achieved whenever $\lambda_b\ll 1$ and $\varepsilon<1$.

To gain physical insight, one may drop the small constant $-\frac{1}{2}$ and $\frac{1}{4}\lambda_b^2$ to obtain a slightly looser but more transparent bound,

$$\langle b_1^\dagger b_1\rangle(T)\lesssim\frac{1}{2}N_b\lambda_b^2+\varepsilon,$$

which is valid for $N_b\gg 1$ and $\lambda_b\ll 1$. This approximate form separates the contributions of the compressed initial thermal excitation $\frac{1}{2}N_b\lambda_b^2$ and the pulse-accumulated noise ε, and it still guarantees ground–state cooling whenever $\frac{1}{2}N_b\lambda_b^2+\varepsilon<1$.

The theorem holds uniformly for all possible initial quantum states because the norm inequality provides a worst-case bound. The intermediate dynamics may exhibit transient oscillations or instantaneous eigenvalue crossings into the right half-plane (as indicated by the counter-rotating terms), yet the global contraction factor λ_b guarantees that no divergence occurs and the net evolution is contractive. This is the mathematical reason why the present pulsed scheme remains stable even in parameter regimes where the conventional Routh–Hurwitz criterion is violated, as discussed in Section 4 of the main text.

A6. Numerical computation of the contraction factor

In practice, λ_b is obtained by numerical integration of Eq. (A11) together with the optimized pulse. The values listed in the last column of Table 1 are all on the order of 10^{-2}–10^{-6}, confirming $\lambda_b\ll 1$ and thus validating the hypothesis of Theorem 1 for all simulated cases.

Acknowledgment

Project supported by the Fundamental Research Funds for the Central Universities (Grant No. 25CAFUC09019).

References

[1] Ranjit G, Cunningham M, Casey K and Geraci A A 2016 *Phys. Rev. A* **93** 053801
[2] Blakemore C P, Rider A D, Roy S, Fieguth A, Kawasaki A, Priel N and Gratta G 2019 *Phys. Rev. Applied* **12** 024037
[3] Xiao W, Liu X, Wu T, Peng X and Guo H 2024 *Phys. Rev. Lett.* **133** 093201
[4] Xu A N, Li Y, Li X, Liu B and Liu Y C 2024 *Phys. Rev. Lett.* **133** 153601
[5] Du L, Monsel J, Wieczorek W and Splettstoesser J 2025 *Phys. Rev. A* **111** 013506
[6] Liu J, Lin Y, Cai H, Chen X, Li N, Hu H and Liu C 2025 *Photonics* **12** 953
[7] Wen P, Wang M and Long G L 2023 *Frontiers in Physics* **11** 1218010
[8] Wang Y D and Clerk A A 2013 *Phys. Rev. Lett.* **110** 253601
[9] Teufel J D, Donner T, Li D, Harlow J W, Allman M S, Cicak K, Sirois A J, Whittaker J D, Lehnert K W and Simmonds R W 2011 *Nature* **475** 359

CPB Online In-Press

[10] Clark J B, Lecocq F, Simmonds R W, Aumentado J and Teufel J D 2017 *Nature* **541** 191
[11] Wang J Q, Zhang A, Tian C C, Yin N, Zhu Q, Wang B, Xiong Z X, He L X and Lv B L 2022 *Chin. Phys. B* **31** 090601
[12] Schliesser A, Rivi'ere R, Anetsberger G, Arcizet O and Kippenberg T J 2008 *Nat. Phys.* **4** 415
[13] Wilson-Rae I, Nooshi N, Zwerger W and Kippenberg T J 2007 *Phys. Rev. Lett.* **99** 093901
[14] Marquardt F, Chen J P, Clerk A A and Girvin S M 2007 *Phys. Rev. Lett.* **99** 093902
[15] Nunnenkamp A, Børkje K and Girvin S M 2011 *Phys. Rev. Lett.* **107** 063602
[16] Monsel J, Ciers A, Manjeshwar S K, Wieczorek W and Splettstoesser J 2024 *Phys. Rev. A* **109** 043532
[17] Wu M, Hryciw A C, Healey C, Lake D P, Jayakumar H, Freeman M R, Davis J P and Barclay P E 2014 *Phys. Rev. X* **4** 021052
[18] Primo A G, Pinho P V, Benevides R, Gröblacher S, Wiederhecker G S and Alegre T P M 2023 *Nat. Commun.* **14** 5793
[19] Gong Z C, Shen C Y, Yuan Q, Sun C P, Li Y and Fu H 2023 *Frontiers in Physics* **11** 1149337
[20] Mancini S, Vitali D and Tombesi P 1998 *Phys. Rev. Lett.* **80** 688
[21] Wodedo M A, Tesfahannes T G, Darge T Y, Bedore M T, Kumela A G and Adera G B 2024 *Scientific Reports* **14** 27234
[22] Zhang H, Qin G Q, Song X K and Long G L 2021 *Opt. Express* **29** 5358
[23] Huang J, Lai D G, Liu C, Huang J F, Nori F and Liao J Q 2022 *Phys. Rev. A* **106** 013526
[24] Xu H, Song X K, Wang D and Ye L 2023 *Science China Physics, Mechanics & Astronomy* **66** 240314
[25] Li X, Chen J and Mu Q 2026 *Chin. Phys. B* **35** 014207
[26] Liao Q, Ouyang S, Cheng S and Cheng Y 2025 *Chin. Phys. B* **34** 044202
[27] Du Y X, Liang Z T, Li Y C, Yue X X, Lv Q X, Huang W, Chen X, Yan H and Zhu S L 2016 *Nat. Commun.* **7** 12479
[28] Zheng W, Zhang Y, Dong Y, Xu J, Wang Z, Wang X, Li Y, Lan D, Zhao J, Li S, Tan X and Yu Y 2022 *npj Quantum Information* **8** 9
[29] Liu Y H, Yin X L, Huang J F and Liao J Q 2022 *Phys. Rev. A* **105** 023504
[30] Song X K, Ai Q, Qiu J and Deng F G 2016 *Phys. Rev. A* **93** 052324
[31] Zhang H, Song X K, Ai Q, Wang H, Yang G J and Deng F G 2019 *Opt. Express* **27** 7384
[32] Wang Y D and Clerk A A 2012 *New J. Phys.* **14** 105010
[33] Sarma B, Busch T and Twamley J 2020 *New J. Phys.* **22** 103043
[34] Hodaei H, Hassan A U, Wittek S, Garcia-Gracia H, El-Ganainy R, Christodoulides D N and Khajavikhan M 2017 *Nature* **548** 187
[35] Mao X, Yang H, Long D, Wang M, Wen P Y, Hu Y Q, Wang B Y, Li G Q, Gao J C and Long G L 2022 *Photonics Research* **10** 2115
[36] Askari B, Dalafi A and Kazemi M 2025 *Annals of Physics* **481** 170157
[37] Wang Y X, Sanavio C and Bernád J Z 2026 *Phys. Rev. A* **113** 023504
[38] Brif C, Chakrabarti R and Rabitz H 2010 *New J. Phys.* **12** 075008
[39] Leng Z, Mundada P, Ghadimi S and Houck A 2023 *Phys. Rev. Applied* **19** 044034
[40] Werschnik J and Gross E K U 2007 *J. Phys. B: Atom. Mol. Opt. Phys.* **40** R175
[41] Caneva T, Calarco T and Montangero S 2011 *Phys. Rev. A* **84** 022326
[42] Yang T, Xiong M, Xue M, Li X and Li J 2025 *Phys. Rev. A* **111** 052617
[43] Müller M M, Said R S, Jelezko F, Calarco T and Montangero S 2022 *Reports on Progress in Physics* **85** 076001
[44] Müller M M, Gherardini S, Calarco T, Montangero S and Caruso F 2022 *Scientific Reports* **12** 21405
[45] Nazir A and McCutcheon D P S 2016 *J. Phys.: Condens. Matter* **28** 103002

CPB Online In Press